Nanostructure and thermal power of highly-textured and single-crystal-like Bi2Te3 thin films

Zhang, Heng; Momand, Jamo; Levinsky, Joshua; Guo, Qikai; Zhu, Xiaotian; ten Brink, Gert H.; Blake, Graeme R.; Palasantzas, George; Kooi, Bart J.

Published in:
Nano Research

DOI:
10.1007/s12274-021-3743-y

Publication date:
2022

Research Article

Nano Research
2022, 15(3): 2382–2390

ISSN 1998-0124 CN 11-5974/O4
https://doi.org/10.1007/s12274-021-3743-y

Nanostructure and thermal power of highly-textured and single-crystal-like Bi_2Te_3 thin films

Heng Zhang (✉), Jamo Momand, Joshua Levinsky, Qikai Guo, Xiaotian Zhu, Gert H ten Brink, Graeme R. Blake, George Palasantzas, and Bart J. Kooi (✉)

Zernike Institute for Advanced Materials, University of Groningen, Nijenborgh 4, 9747 AG Groningen, The Netherlands

Received: 23 March 2021 / **Revised:** 7 July 2021 / **Accepted:** 15 July 2021

ABSTRACT

Bi_2Te_3-based alloys are known to have outstanding thermoelectric properties. Although structure–property relations have been studied, still, detailed analysis of the atomic and nano-scale structure of Bi_2Te_3 thin film in relation to their thermoelectric properties remains poorly explored. Herein, highly-textured (HT) and single-crystal-like (SCL) Bi_2Te_3 films have been grown using pulsed laser deposition (PLD) on Si wafer covered with (native or thermal) SiO_x and mica substrates. All films are highly textured with *c*-axis out-of-plane, but the in-plane orientation is random for the films grown on oxide and single-crystal-like for the ones grown on mica. The power factor of the film on thermal oxide is about four times higher (56.8 $\mu W \cdot cm^{-1} \cdot K^{-2}$) than that of the film on mica (12.8 $\mu W \cdot cm^{-1} \cdot K^{-2}$), which is comparable to the one of the polycrystalline ingot at room temperature (RT). Reduced electron scattering in the textured thin films results in high electrical conductivity, where the SCL film shows the highest conductivity. However, its Seebeck coefficient shows a low value. The measured properties are correlated with the atomic structure details unveiled by scanning transmission electron microscopy. For instance, the high concentration of stacking defects observed in the HT film is considered responsible for the increase of Seebeck coefficient compared to the SCL film. This study demonstrates the influence of nanoscale structural effects on thermoelectric properties, which sheds light on tailoring thermoelectric thin films towards high performance.

KEYWORDS

Bi_2Te_3 films, highly-textured structure, single-crystal-like structure, thermoelectric properties, pulsed laser deposition

1 Introduction

Bi_2Te_3-based alloys have been intensively investigated over the past decades for their high thermoelectric performance around ambient temperature in converting temperature gradient into voltage, or vice versa [1–5]. The figure of merit, $ZT = S^2\sigma T/k$, is commonly used to evaluate the thermoelectric properties of materials, where S, σ, T, and k are the Seebeck coefficient, electrical conductivity, absolute temperature, and thermal conductivity, respectively [6]. It is generally accepted in the thin film research community that it is challenging to measure the thermal conductivities of films accurately, specifically when the thickness of the film is only a few tens of nanometers. Compared with the bulk of Bi_2Te_3-based alloys, there is no significant advantage for the power factors ($S^2\sigma$) of corresponding thin films, but they still attract great attention due to their potential application in micro/nano-electronics [7]. In order to improve the thermoelectric performance of thin films, numerous studies focused on the impact of microstructures, compositions, morphologies, annealing temperature, thickness as well as different architectures on the thermoelectric properties of Bi_2Te_3 films [8–14]. For instance, in a series of impure Bi-Te films with different thickness, the highest power factor at room temperature (RT) of 18.5 $\mu W \cdot cm^{-1} \cdot K^{-2}$ was achieved [15]. Le et al. and Bassi et al. deposited Bi_2Te_3 films, showing different morphologies when imaged by scanning electron microscopy (SEM), where the power factor was enhanced in films with a layered structure [9, 10]. Furthermore, utilizing irradiation, Suh et al. obtained more defective Bi_2Te_3 films which significantly improved the power factor to a value as high as 34 $\mu W \cdot cm^{-1} \cdot K^{-2}$ [13]. Indeed, except for doping, defect engineering by introducing point defects, dislocations, grain boundaries, and nano-inclusion is another powerful method in obtaining high performance thermoelectric materials.

Bi_2Te_3 films with textured microstructure remarkably enhance the power factor as the carrier mobility and electrical conductivity show superior behavior along the *ab*-plane. However, due to the difficulty to grow highly-textured (HT) films, previous studies on the textured Bi_2Te_3 films have mostly focused on (000*L*) textured film with some other orientations [8, 16]. Only a few reports have been found, where exclusive (000*L*) orientated films were grown to improve the power factor [9, 17]. Zhang et al. fabricated the highly-textured Bi_2Te_3 film with columnar nanostructure by sputtering, which simultaneously improved the electrical conductivity and Seebeck coefficient [17]. On the other hand, it is also reported that the power factor could be notably increased because of low-angle grain boundaries even though the Seebeck coefficient slightly decreased in Bi_2Te_3 film with well-ordered structure [18]. Clearly, in order to enhance the electrical conductivity, it is necessary to grow well-textured films, but

Address correspondence to Heng Zhang, heng.zhang@rug.nl; Bart J. Kooi, b.j.kooi@rug.nl

whether the Seebeck coefficient can be properly tailored with such structure is still ambiguous. Therefore, in-depth research on the microstructure in these well-ordered Bi_2Te_3 films is necessary to figure out solutions for further optimizing their thermoelectric properties. It should be noted that with sputtering it is difficult to control the film quality in spite of its wide use in industrial fabrication lines. Recently, a two-step process was employed to grow highly-textured two-dimensional (2D) chalcogenide films in sputtering and molecular beam epitaxy (MBE) systems [19, 20]. Intriguing phenomena were found based on this highly-textured structure. Saito et al. observed zero-band gap in highly-textured Bi-rich Bi-Te films by optical measurements [21]. Taskin et al. fabricated high-quality epitaxial Bi_2Se_3 films with various thicknesses using a similar strategy by MBE, where topological protection was confirmed below the thickness of ~ 6 nm [22]. In our previous studies, we also succeeded in depositing highly-textured chalcogenide films on amorphous SiO_x surface by this two-step growth process with pulsed laser deposition (PLD) [23, 24]. Herein, we have grown highly-textured Bi_2Te_3 films on amorphous SiO_x surface and crystalline mica surface by the two-step and a one-step process, respectively. In previous research, clear relations between thermoelectric properties and factors like thin film morphologies and texture, annealing temperature, and thickness have been shown [9, 16–18]. However, these previous studies in general lacked comprehensive analyses of atomic scale structure effects on thermoelectric properties. The aim of this work is to add these atomic scale structure details and to improve our understanding of how to control and optimize the power factor using the nanoscale structure of thin films.

2 Experimental

Bi_2Te_3 films were grown on Si (100) covered with native oxide (~ 1.8 nm, Fig. S1 in the Electronic Supplementary Material (ESM)), Si (100) covered with thermal oxide (~ 300 nm), and freshly cleaved (001) muscovite mica substrates by PLD using a commercial stoichiometric compound target obtained from KTECH with a purity of 99.999%. The native Si (100) and thermal Si (100) substrates were sonicated in acetone, isopropanol, and ethanol, and then dried using a nitrogen jet before being glued on the deposition stage. A two-step growth method was used to grow Bi_2Te_3 films on native and thermal oxide. During deposition, firstly a "seed" layer of 200 pulses (~ 3 nm) Bi_2Te_3 film was grown at RT, and heated at 10 °C·min^{-1} to 210 °C. Then 1,800 pulses (~ 27 nm) Bi_2Te_3 film was deposited at 210 °C. Once cleaved in air, the mica substrate was immediately installed in the PLD chamber and heated at 10 °C·min^{-1} to 210 °C, followed by 2,000 pulses Bi_2Te_3 film deposition. All the depositions were done using a KrF laser (λ = 248 nm) in an Ar gas ambient at a pressure of 0.12 mBar with a 1 sccm flow. The background pressure was below 10^{-7} mBar and the distance between target and substrate was 5 cm. The deposition was carried out with a laser fluence and repetition of 0.8 J·cm^{-2} (spot size 1.3 mm^2) and 1 Hz, respectively. After deposition, the heater was turned off, Ar gas was pumped out, and the samples were cooled down to RT in the chamber (pressure below 10^{-6} mBar).

The crystalline structure of the Bi_2Te_3 films was assessed by X-ray diffraction (XRD), using a Panalytical X'pert Pro diffractometer operating with high-resolution θ–2θ specular scans and ω-rocking scans. Surface morphology was characterized by atomic force microscopy (AFM), using a Bruker MultiMode 8 and analyzed by the Gwyddion software. *In situ* reflection high-energy electron diffraction (RHEED) was used to observe the top surface structure during the deposition. Transmission electron microscopy (TEM) cross-section samples were prepared by a focused ion beam (FIB, Helios G4 CX DualBeam™). The preparation of the mica plan-view specimen is detailed in a previous publication [24]. S/TEM measurements were performed with a probe- and image-corrected Thermo Fisher Scientific Themis Z S/TEM operating at 300 kV. The plan-view specimen on Si wafer were prepared by mechanical polishing, dimple grinding, followed by low-voltage Ar^+-ion milling for final thinning using a Gatan PIPS II to achieve electron transparency. Part of TEM analysis and corresponding selected area electron diffraction (SAED) were carried out using a JEOL 2010 TEM operating at 200 kV. Seebeck coefficients and electrical conductivity were measured using a Linseis LSR-3 apparatus and the van der Pauw method, respectively.

3 Results and discussion

Significant efforts were devoted to optimizing the deposition parameters for pure Bi_2Te_3 [12, 16]. Due to the anisotropic trigonal structure, the crystal orientation of Bi_2Te_3 film must be controlled to achieve desirable thermoelectric properties. RHEED patterns recorded during the optimized growth process of the Bi_2Te_3 films on the three types of substrates (native silicon oxide, thermal silicon oxide, and mica) are shown in Fig. 1. During the two-step growth process, a direct change from the substrate pattern to a *c*-axis textured polycrystalline Bi_2Te_3 film pattern is observed for both the native and thermal oxide substrates (the left two columns in Fig. 1). Since only a very thin SiO_x layer on top of the native substrate is present, a relatively weak dotty RHEED pattern with Kikuchi lines of Si (001) can be detected. When the SiO_x layer becomes thicker, like ~ 300 nm for the thermal oxide, RHEED electrons cannot penetrate through the amorphous oxide film and a typical hazy pattern is generated as depicted in Fig. 1(a) (the Thermal column). When the 200 pulses Bi_2Te_3 seed layer is

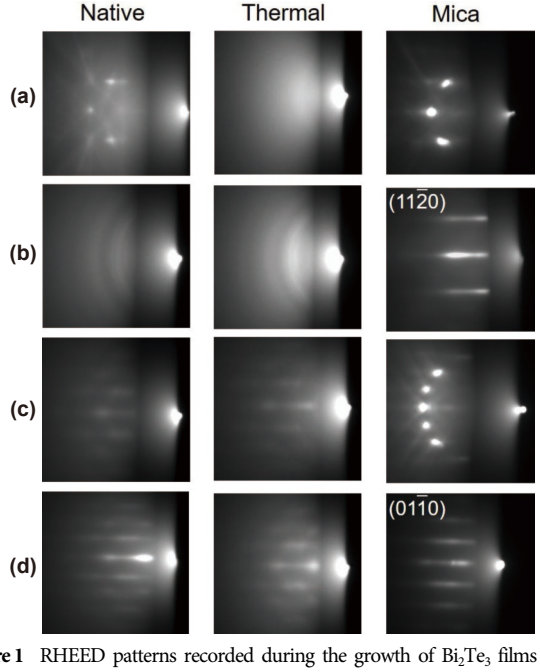

Figure 1 RHEED patterns recorded during the growth of Bi_2Te_3 films on Si (100) containing native oxide (left column), thermal oxide (middle column), and on mica (right column). The Native and Thermal columns show the bare substrates in (a) 200 pulses Bi_2Te_3 seed layer deposited at RT (b) and after heating to 210 °C (c), and Bi_2Te_3 surface at the end of the (in total 2,000 pulses) growth (d). (a) The Native column shows that the penetration depth of RHEED is still sufficient for reaching the Si (100) substrate. The Mica column shows RHEED patterns from the bare mica (a) and as-deposited Bi_2Te_3 film (b) perpendicular to mica < 1$\bar{1}$0 > and Bi_2Te_3 < 11$\bar{2}$0 >, respectively. (c) and (d) are patterns taken from bare mica and as-deposited Bi_2Te_3 film perpendicular to mica <010> and Bi_2Te_3 < 01$\bar{1}$0 >, respectively.

grown on the native and thermal oxide substrates, their RHEED patterns change to blurry rings (Fig. 1(b), the Native and Thermal columns), which indicate that the RT growth of Bi_2Te_3 is not fully amorphous but contains some (nano)crystalline constituents. Figure 1(c) (the Native and Thermal columns) shows that by annealing at 210 °C, the Bi_2Te_3 seed layer is transformed into a fully crystalline film with minor (atomic scale) roughness as can be derived from the streaky pattern [25]. The roughness is not substantial, because then a so-called three-dimensional (3D) pattern would be observed, i.e., with distinct spots on multiple rings [26]. With further deposition of Bi_2Te_3 at high temperature in Fig. 1(d) (the Native column), the streaky features become more apparent, because the diffuse intensity around the streaks from the annealed seed layer has largely vanished, showing that the crystal quality of the film surface improves during the growth. However, in Fig. 1(d) (the Thermal column), the streaky intensity also increases, but the diffuse intensity around the main streaks remains similar, which implies that a considerable amount of defects is generated during the growth process and substantial disorder remains present during growth at the surface. Without such defects, the diffuse intensity should have largely vanished and this is not observed. The distances between the streaks in all cases correspond to the expected interplanar distances in the basal plane, showing that the films have their *c*-axis out-of-plane. Since it is also found that the RHEED patterns do not change upon rotation for both native and thermal oxide substrates, the in-plane orientation is random, indicating domains with *c*-axis out-of-plane but not any texture in-plane. Probably the domain structure in these Bi_2Te_3 films is very similar to the one in Sb_2Te_3 we analyzed earlier in more detail with transmission electron backscatter diffraction (see Fig. 4 in Ref. [27]).

On the other hand, when Bi_2Te_3 is grown on bare mica heated at 210 °C, the spot pattern from smooth mica immediately gives way to a nice sharp streak pattern from Bi_2Te_3. Also, when rotating the mica in-plane from $<1\bar{1}0>$ to <010>, the corresponding in-plane crystal direction of the Bi_2Te_3 film changes from $(11\bar{2}0)$ to $(01\bar{1}0)$, as can be observed from comparing the Mica column in Figs. 1(a)–1(d). Therefore, it can be stated that the Bi_2Te_3 films on mica not only have *c*-axis out-of-plane, but also are highly textured in-plane, pointing at a single-crystal-like (SCL) structure. Based on RHEED only, it cannot be proven whether the film has a single crystal structure or consists of domains with small-angle misorientation, but the XRD and TEM results presented below will shed more light on this.

Results of XRD analyses of the (2,000 pulses) Bi_2Te_3 films on the three types of substrates are shown in Fig. 2. It can be noticed readily that, in addition to the substrate (Si and mica) peaks, only the Bi_2Te_3 (000*L*) (*L* = 3, 6, 15, 18, 21) Bragg peaks can be detected, indicating that all films were grown highly textured with *c*-axis out-of-plane without any observable impurity phase. Since the *c* lattice parameter of mica is nearly twice as large as the Bi_2Te_3 quintuple distance, the mica (00*L*) peaks are close to the Bi_2Te_3 (000*L*) peaks. For instance, the strongest Bi_2Te_3 (0006) peak overlaps with the mica (004) peak. It has been shown earlier that highly textured 2D thin films can be fabricated by utilizing self-oriented seed layers (using the so called two-step process) [23, 27]. Since we use the same method to grow Bi_2Te_3 films on native and thermal oxide substrates, which have the same chemical amorphous surface (SiO_x), the same final film quality is expected. However, in the case of the native oxide, we found slightly weaker and broader XRD peaks (as well as lower signal-to-noise ratio in the XRD spectra). On the other hand, the Bi_2Te_3 on the mica sample shows the sharpest XRD peaks. In order to quantify the degree of out-of-plane texture, ω rocking scans are shown in Fig. 2(b). The full-width-at-half-maximum (FWHM) values of the

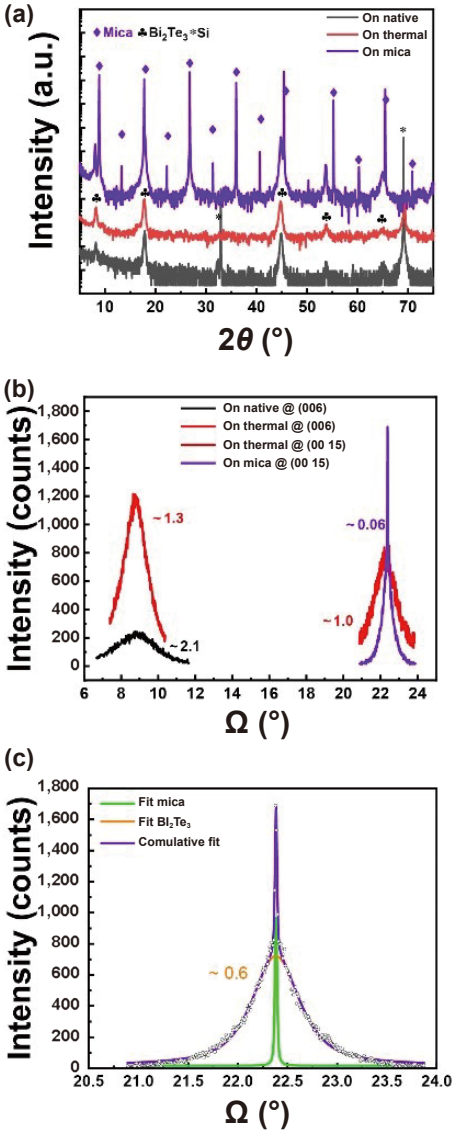

Figure 2 (a) θ–2θ XRD scans of Bi_2Te_3 films on three different substrates at 210 °C, (b) ω-scans of Bi_2Te_3 (0006) reflection on native and thermal oxide substrates, and ω-scans of Bi_2Te_3 (000 15) reflection on thermal oxide and mica substrates. (c) The fitting of ω-scan around the Bi_2Te_3 (000 15) peak on mica substrate. Numbers in (b) and (c) are the full width at half maximum values of the corresponding curves.

Bi_2Te_3 (0006) peaks from the ω-scans (~ 1.3° versus ~ 2.1°) clearly corroborate that the out-of-plane texture is sharper for the Bi_2Te_3 on thermal oxide than on native oxide. ω-scans of the Bi_2Te_3 (000 15) peaks imply that the orientation on mica is even better than on thermal oxide (~ 0.6° versus ~ 1.0°), although a one-step growth process is used in the former case and a two-step process in the latter case. When analyzing the ω-scan for the sample on mica, the rocking curve actually consists of two different peaks: a broad peak from the Bi_2Te_3 film and a narrow peak from the mica. This can reasonably explain why the overall curve exhibits a much smaller tilt distribution (~ 0.06°) compared with MBE grown films [28–30]. However, this ~ 0.06° is an erroneous value for evaluating the texture of Bi_2Te_3 on mica, because firstly the mica peak must be removed. In order to do so, the FWHM of the bare mica peak was measured to be 0.027° (Fig. S2 in the ESM). For the overall fit, PsdVoigtI functions were used, where the FWHM of the narrow mica peak was fixed and the peak positions of the narrow and broad peaks were shared when fitting the Bi_2Te_3 (000 15) peak. The R-square value of the fit is 0.992, showing that the data is

fitted well. The FWHM of the remaining pure Bi_2Te_3 (000 15) peak is actually ~ 0.6°. Still, it demonstrates that the out-of-plane mosaic spread is the smallest for the film deposited on mica.

The topographies of the Bi_2Te_3 films on the different substrates were measured by AFM (Fig. 3). The root-mean-square (RMS) roughness of the 2,000 pulses Bi_2Te_3 film on native and thermal oxide substrates is determined to be ~ 1.5 and ~ 1.2 nm, respectively. It should be noted that, even when the film on thermal oxide is slightly thicker than the one on native oxide (~ 32.4 versus ~ 31.3 nm, Fig. S3 in the ESM; thicknesses were measured based on FIB prepared cross-sections imaged using SEM), the surface is still smoother, which is another hint that the mosaicity of the Bi_2Te_3 film on thermal oxide substrate is smaller. This is in agreement with the XRD results shown in Fig. 2. In comparison, a much lower RMS roughness of ~ 0.35 nm is derived for ~ 24.6 nm Bi_2Te_3 film on mica (Fig. S3 in the ESM). Such a smooth and high quality film is comparable to the MBE-grown Bi_2Te_3 film [29, 31].

The local atomic structure of the Bi_2Te_3 films has been studied using S/TEM, of which overview plane-view and cross-section images of the Bi_2Te_3 film on native oxide are shown in Figs. 4(a) and 4(b), respectively. Combining the plane-view image and correlated SAED pattern shown as inset, the random in-plane Bi_2Te_3 crystal orientation and domain boundaries are clearly observable. The rings in the SAED pattern, indicating the random in-plane orientation, originate from the Bi_2Te_3 film. However, the four distinct sharp spots originate from the Si (100) substrate (showing 4 {022} reflections) below the thin native oxide. The

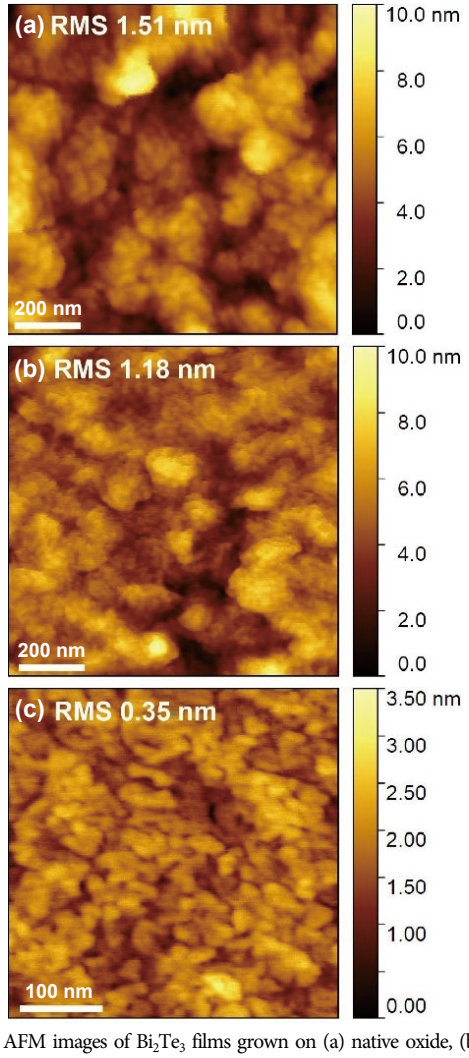

Figure 3 AFM images of Bi_2Te_3 films grown on (a) native oxide, (b) thermal oxide, and (c) mica substrates.

interaction between the Si substrate and the Bi_2Te_3 gives rise to double diffraction in the SAED pattern. In addition, interesting growth features can be observed in this two-step growth on the native oxide. The smallest domain size found in the plan-view images is ~ 50 nm, which is clearly bigger than the film thickness. So, it is expected that the domain boundaries would run across the entire film thickness and would not be parallel to the film surface. This is widely found in many thin films [27, 32]. In this respect, Fig. 4(b) shows that two domains stack on top of each other, where the domain boundaries are indicated by the green dash line. Such special domain boundaries have also been found in MBE-grown Bi_2Te_3 film on Si substrate [33]. This explains, at least in part, why mosaicity of Bi_2Te_3 film on native oxide substrate is relatively large, even though tilted domains creating clear surface roughness like in Sb_2Te_3 film grown with physical vapor deposition (PVD) and Ge-Sb-Te film grown with PLD are not observed in this case [34, 35]. A typical high-angle annular dark-field scanning TEM (HAADF-STEM) image of columnar domains with hexagonal crystal structure is shown in Fig. 4(c). It shows that the tilt distribution of neighboring domains is so limited that van der Waals (vdW) gaps of the left domain are aligned parallel to the right one. Since the left one is not viewed along a zone axis, the atomic columns are invisible. In contrast, a nice stack of quintuples is observable in the domain on the right, from which the extracted local line-scan depicted in Fig. 4(e) shows the [–Te^1–Bi–Te^2–Bi–Te^1–] quintuple structure well. Also, the vdW gaps between [Te^1–Te^1] are clearly present as indicated by the orange arrows in Fig. 4(e). Nevertheless, abundant bilayer defects are seen throughout the entire film, where examples are shown in Fig. 4(d) and indicated by the yellow and red dash lines. This kind of defect was previously reported in GeSbTe film/superlattice on etched Si surface, and ascribed to the effect induced in the film by a monolayer surface step on the substrate [35]. However, this cannot directly explain the bilayer defects in the film analyzed here, because the native oxide at the surface is amorphous. Still, the native oxide is so thin (~ 1.8 nm) that it cannot fully smoothen the atomic steps at the Si (100) surface. Then, when domains nucleate and grow on different locations with slightly tilted orientation, their vdW gaps do not align perfectly at the domain boundaries. Bilayer defects then still arise to accommodate the misalignment at the domain boundaries. Considering defect engineering (nano-inclusion), which is a promising route to obtain high *ZT* values in bulk materials as well as thin films [36, 37], we anticipate relatively good performance of this film. However, since the native oxide is so thin, it is not possible to measure thermoelectric properties of solely the Bi_2Te_3 film due to interference of the Si substrate. This is rather unfortunate, because potentially the power factor of the Bi_2Te_3 film on native oxide could be better than the ones measured for the films on thermal oxide and mica.

Next we study the local nanostructure of Bi_2Te_3 films on thermal oxide in an analogous manner as done for the film on the native oxide. Exemplary results are depicted in Fig. 5. Also herein, Fig. 5(a) and the inset show the plan-view TEM image and corresponding SAED pattern, and Fig. 5(b) shows the overview HAADF-STEM image of cross-sectional Bi_2Te_3 film. The morphology is similar to the film on the native oxide, whereas the SAED pattern only shows four rings resulting from diffraction of Bi_2Te_3 (110), (300), (220), and (410) planes. The double diffraction is invisible, from which we can directly deduce that there is only SiO_x beneath the Bi_2Te_3 films. The domain size shown in Fig. 5(b) is ~ 90 nm, in agreement with the size range from ~ 60 to ~ 200 nm measured from Fig. 5(a). The overview HAADF-STEM image also shows, analogous to the Bi_2Te_3 layers on the native oxide, a relatively flat film with properly organized quintuple structures. It

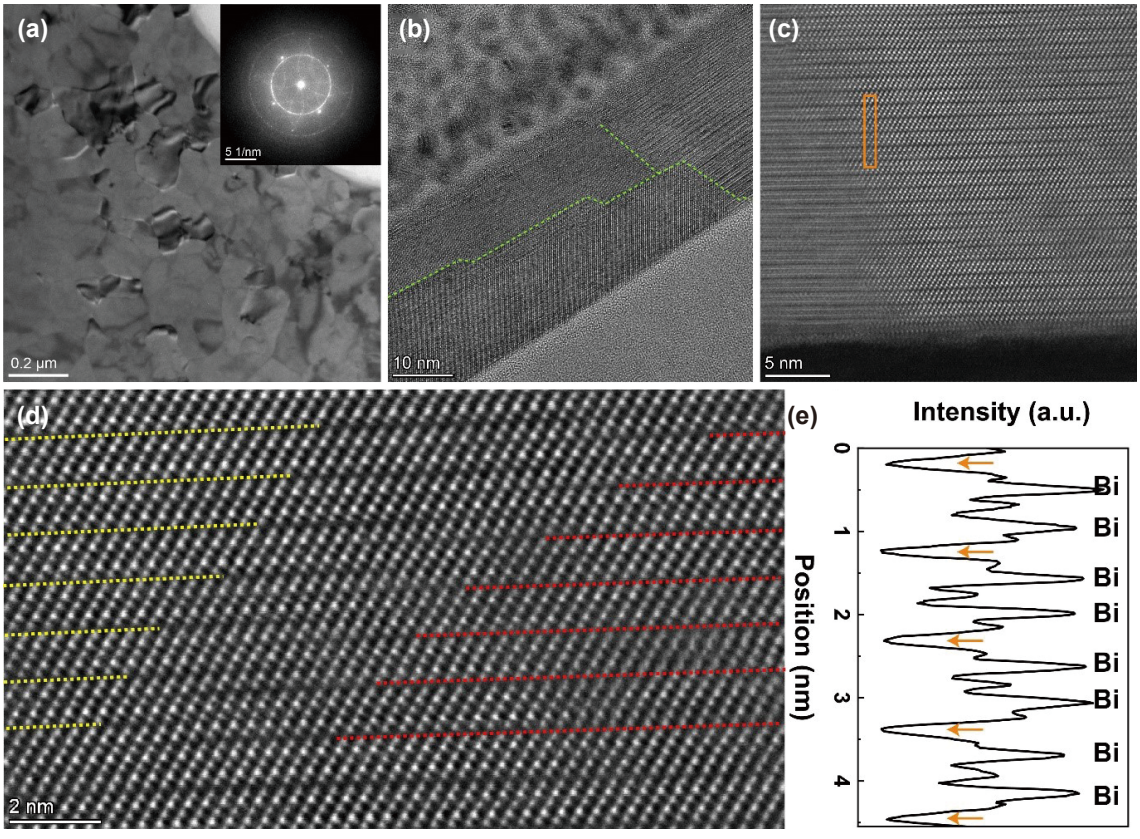

Figure 4 S/TEM analysis of Bi_2Te_3 film grown on native oxide. (a) Bright-field TEM image of plan-view Bi_2Te_3 film. The inset shows the SAED pattern. (b) Overview bright-field TEM image of cross-sectional Bi_2Te_3 film. (c) HAADF-STEM image around a boundary between well-aligned domains. (d) High-resolution HAADF-STEM image around a boundary with slightly misaligned domains, showing bilayer defects. The yellow and red dash lines show the vdW gaps in both domains. (e) Intensity line-scan from the area shown in (b) demonstrates the perfect quintuple stacking in local regions. The vdW gaps are indicated by the orange arrows.

is noteworthy to mention that, in contrast to the film on the native oxide, overlapping domains stacked on top of each other are not detected for the film on the thermal oxide. Probably this relates to the observation that the *c*-axis out-of-plane texture is somewhat sharper on the thermal oxide substrate than it is on the native oxide substrate. However, different situations can be observed along the domain boundary shown in Fig. 5(c). The first situation is that most of the vdW gaps in the right domain are not aligned with the ones in the left domain, which may cause mutual interaction between these domains. Similar bilayer defects, as already presented for the Bi_2Te_3 film on the native oxide sample, can also be found here for the thermal oxide sample where an example is indicated by the yellow arrow. However, in addition, it is observed that many vdW gaps cannot extend to the boundary forming regular bilayer defects as in Fig. 4(d). An example is singled out by the yellow ellipse. Probably the interaction between the domains at the boundary causes additional stacking disorder close to boundary. In a previous result, Ross et al. show that GeSbTe films grown by PLD contain a considerable amount of disordered stacking sequences which may be ascribed to local composition fluctuations [35]. Although this is more likely for a ternary alloy, it is still possible that the local variations in Bi to Te ratio cause stacking disorder.

The RHEED patterns of the Bi_2Te_3 film grown on mica clearly demonstrate that this type of film is also highly-textured in-plane. However, from the AFM image it remains unclear what the exact nature is of the domain boundaries. This is important for the thermoelectric properties which are influenced by scattering of the free charge carriers and by phonon propagation through the structure [18]. In order to investigate the boundaries in more detail, three different TEM-based methods were used to distinguish them at different locations. Each method was applied to several boundaries and representative results are depicted in Fig. 6. First we exploited a small selected area aperture to obtain SAED pattern around a domain wall, as indicated by the purple circle in the bright-field image shown in Fig. 6(a). The corresponding SAED pattern along the [0001] zone-axis confirms one set of sharp six fold symmetric diffraction dots, not revealing any small misorientation between the neighboring domains. In case there is a tiny misorientation, maybe SAED does not have the required precision and, therefore, atomic resolution HAADF-STEM images across domain boundaries are also acquired. Figure 6(b) shows an example of the image where we can find "strong" boundaries and "weak" boundaries. In particular, some "weak" boundaries evolve to inside the domain and then vanish at some point. The inset shows the fast Fourier transform (FFT) of the image, where homologous reflections are found, further verifying that a misorientation is not observable. Note that random Moiré interferences are present in the high resolution transmission electron microscopy (HRTEM) image of the sample shown in Fig. 6(c), due to transmission trough surface oxidized layer and Bi_2Te_3 crystals, but not through Bi_2Te_3 and mica crystals, which would give rise to one specific Moiré pattern. It was previously found that the top quintuple layer could be oxidized after a few days [38]. Therefore, in order to minimize the influence of the oxidation, in subsequent measurements, fresh samples were used, i.e., analyzing them as soon as possible after taking them out of the PLD chamber. The third method used here to study domain boundaries is focusing on the atomic resolution HAADF-STEM images around the boundary. The top left overview image in Fig. 6(d) shows the locations at the boundary where the more detailed atomic resolution images in the red box showing a "strong" boundary and the yellow box showing a "weak" boundary are taken. From the atom planes on both sides of the

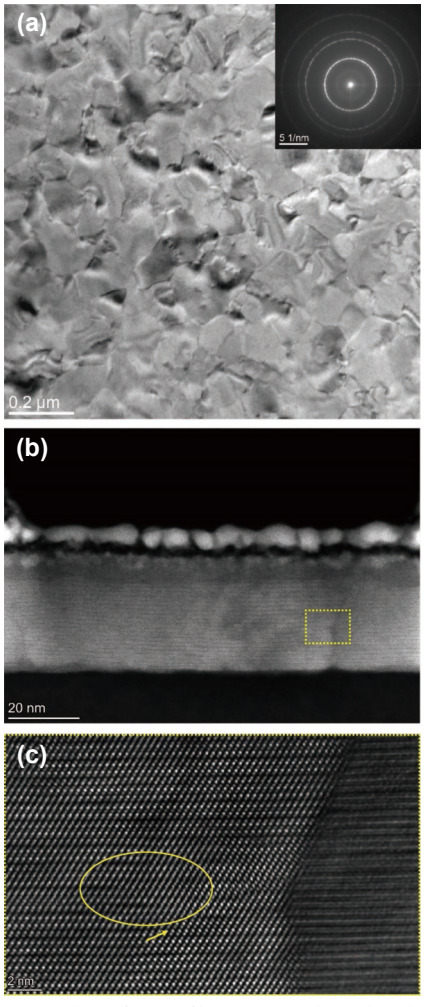

Figure 5 S/TEM analysis of Bi_2Te_3 film grown on thermal oxide substrate. (a) Bright-field TEM image of plan-view Bi_2Te_3 film. The inset shows the SAED pattern. (b) Overview HAADF-STEM image of cross-sectional Bi_2Te_3 film. (c) A magnified image of the yellow rectangle area indicated in (b), showing considerable stacking disorder in the domain on the left close to a domain boundary.

boundary, it can now be observed that the planes are well aligned across the boundary, although there is a thin zone with hardly recognizable atomic structure at this "strong" boundary. For the "weak" boundary, however, this atomic structure is even clearly visible at the boundary. So, the above three types of results clearly demonstrate that the boundaries do not exhibit an observable rotation around the out-of-plane direction, but must originate from a small out-of-plane misalignment, e.g., due to the stacking disorder in out-of-plane direction or a slight rotation around an in-plane axis. In our previous study, we also discovered that bilayer defects exist already in a very thin Bi_2Te_3 layer on mica [24]. However, the Bi_2Te_3 films on mica for TEM investigation were floated off the mica and then scooped up and collected on a TEM grid. During this process, some bending of the film can occur and induce or aggravate the boundaries by inducing a slight rotation around an in-plane axis. Nevertheless, since boundaries are observed by AFM for films still on the substrate, it is not possible that all boundaries are an artifact of TEM sample preparation. Still, the most striking difference between the Bi_2Te_3 films on amorphous silicon oxide and mica is related to the in-plane stacking. All are highly-textured out-of-plane, but on the oxide substrates the films have domains with random orientation in-plane, whereas on mica the film is SCL with even single orientation in-plane.

An important final goal of the present work is to correlate the detailed nanostructural observations of the different types of Bi_2Te_3 films shown above with their thermoelectric properties. In particular, whether a significant difference in properties can be observed for the HT films (with domains with random in-plane orientation) and SCL films? Although the electrical conductivity (σ) and Seebeck coefficient (S) of Bi_2Te_3 films have been studied, including thick HT Bi_2Te_3 films, no results have been reported on such "thin" films with these specific detailed known structures. Figures 7(a) and 7(b) present, for the temperature range from 30 to 210 °C, the change of σ and S, respectively. With the increase of temperature, the in-plane σ values of both the HT and SCL films decrease, while the absolute S values increase. The σ results demonstrate that both types of Bi_2Te_3 films exhibit typical metallic-like behavior, because it is dominated by a reduced charge carrier mobility due to the well-known scattering effects between carriers, phonons, and defects. The negative values measured for the Seebeck coefficient for both types of films show that the dominant charge carriers in our Bi_2Te_3 film are electrons. The results show that the Bi_2Te_3 in our films is a degenerate n-type semiconductor. A very prominent observation is that the σ of the SCL film is much higher than that of highly-textured film, e.g., about 2,440 and 1,980 $S{\cdot}cm^{-1}$ at RT, which is ~ 23% higher (see Fig. 7(a)). It has been proved that the carrier concentration in well-ordered Bi_2Te_3 film (~ 5–6 × 10^{20} cm^{-3}) is lower than in random-ordered film (~ 8–9 × 10^{20} cm^{-3}), but the carrier mobility is about a factor of two higher, comparing the power factor with previously reported [18]. Such a SCL structure can explain well the relatively high carrier mobility in the film, because, as shown by Fig. 6, crystal planes are perfectly aligned (even across domain boundaries) over large distances in the in-plane direction which is the direction in which the conductivity is measured and which thus leads to high electrical conductivity. On the other hand, the domains in the HT films on thermal oxide have random in-plane orientation and have sizes of only 60–200 nm. These domain boundaries give rise to substantially more charge carrier scattering and thus reduced mobility and conductivity. In contrast to the ~ 23% lower conductivity, the Seebeck coefficient measured at RT for the HT film is two times higher than the one for the SCL film (see Fig. 7(b)). When the temperature increases to ~ 210 °C, it even becomes ~ 3.5 times higher. The relevant reason is probably the more pronounced scattering in the HT film. Assuming a Boltzmann distribution for the electrons, the S at RT depends on the scattering parameter (s) and carrier concentration (n), as expressed below [39]

$$S = \frac{K_B}{e}\left[s + \frac{5}{2} + \ln\frac{2(2m^* K_B T)^{\frac{3}{2}}}{nh^3}\right] \quad (1)$$

where e is the electronic charge, K_B is the Boltzmann constant, m^* is the effective mass of the charge carrier, and h is Planck's constant. The scattering parameter s is based on the relaxation time for the charge carriers. In general, there are several scattering mechanisms, i.e., phonon scattering, alloy scattering, ionized impurity scattering, and carrier scattering. Compared with the SCL film, the in-plane orientation of HT film is random and more stacking and layering faults can be observed in the film, particular high-density line defects close to boundaries, which generate more scatterings and probably cause the film to exhibit high Seebeck coefficients. Herein, the difference of carrier concentration between the Bi_2Te_3 films with different structure is not expected to be a dominant factor, which is also seen in previous work on the textured Bi_2Te_3 films [17, 40]. Furthermore, a similar mechanism has been found in irradiated (defective) Bi_2Te_3 film, where a transition from phonon-dominated scattering towards impurity-dominated scattering was found, leading to a dramatic

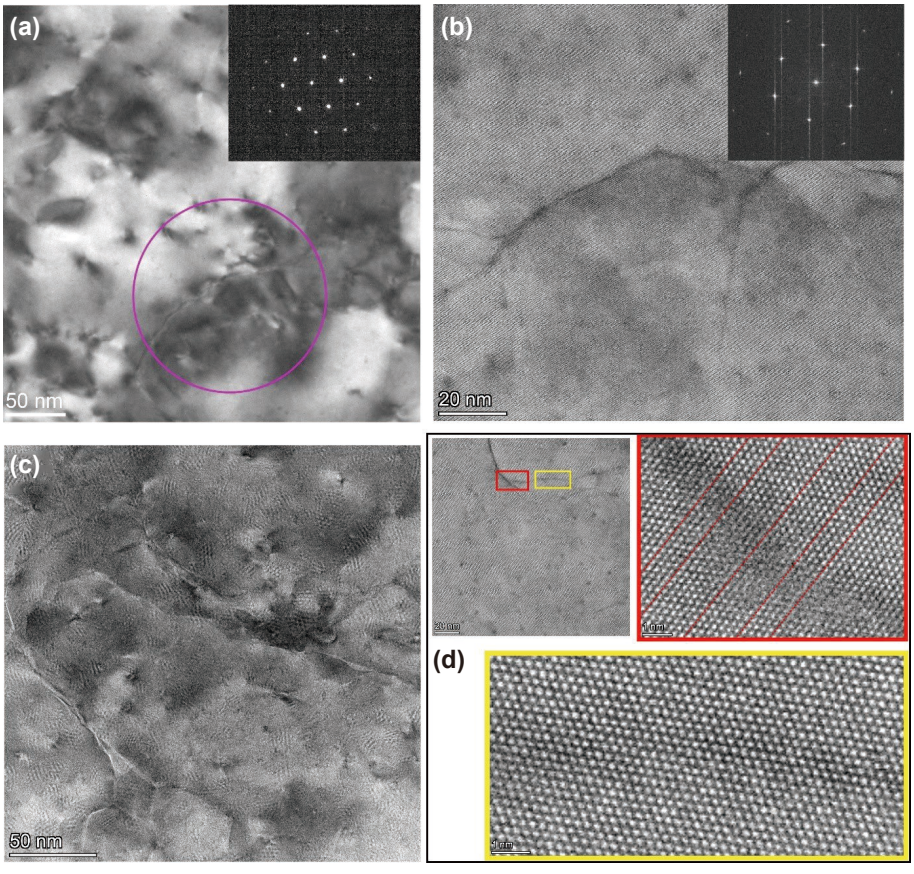

Figure 6 S/TEM analysis of Bi_2Te_3 film on mica substrate. (a) Bright-field TEM image of plan-view Bi_2Te_3 film. The inset shows the SAED pattern taken across two neighboring domains, where the aperture location is indicated by the purple circle in the TEM image. (b) HAADF-STEM image of plan-view Bi_2Te_3 film, showing the branches of domain boundary. The inset shows the FFT from the domains in the image. (c) A wide-area HRTEM image of Bi_2Te_3 film where random Moiré interferences can be observed, indicating the surface of Bi_2Te_3 film has been oxidized. Figures on the top right and bottom in (d) show the atomic HAADF-STEM images crossing the domains of the red and yellow areas indicated in the overview image shown in (d) at the top left.

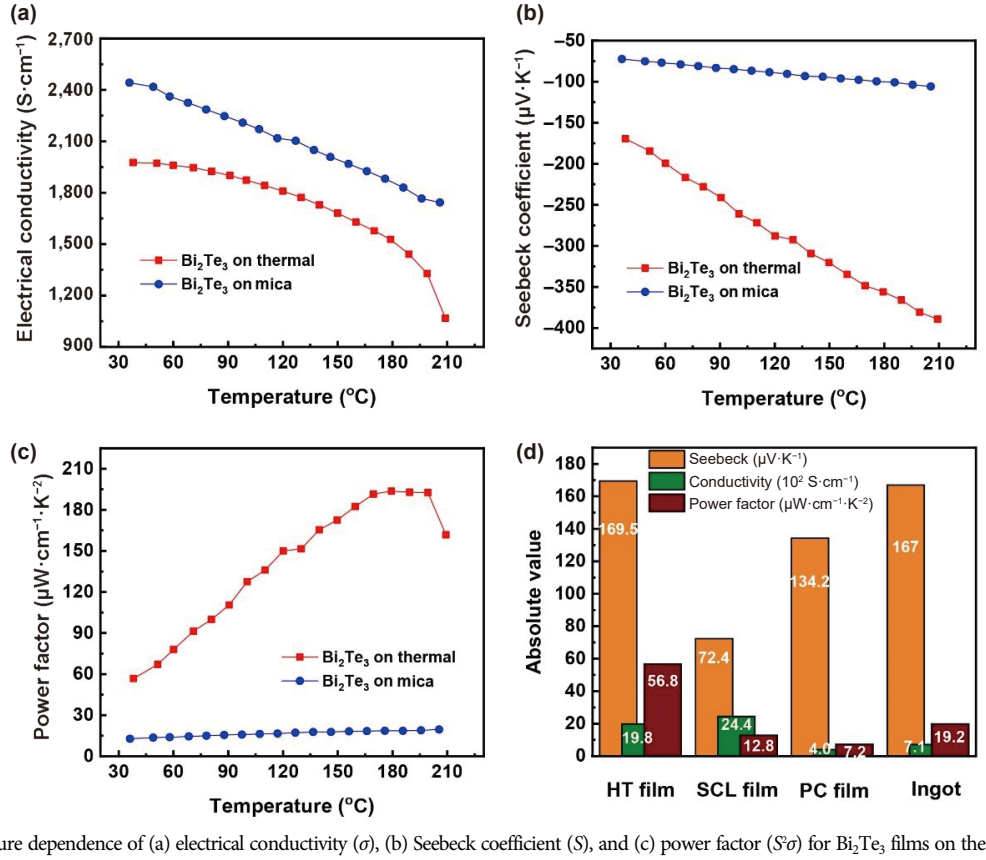

Figure 7 Temperature dependence of (a) electrical conductivity (σ), (b) Seebeck coefficient (S), and (c) power factor ($S^2\sigma$) for Bi_2Te_3 films on thermal oxide and mica substrates. (d) Comparison of in-plane S, σ, and $S^2\sigma$ at RT for highly textured (HT) film, single-crystal like (SCL) film obtained in present work with literature results for polycrystalline (PC) film [17] and polycrystalline ingot [44], respectively.

improvement of the Seebeck coefficient, so that high thermopower was achieved [13]. Also in bulk materials, e.g., based on Mg_3Sb_2 [41], a high Seebeck coefficient could be realized by defect engineering. Since the thermal expansion of mica and Bi_2Te_3 is different, cycles were performed on mica sample (Fig. S4 in the ESM), which indicate good thermal stability of our film. Figure 7(c) shows the corresponding power factors of the films. Owing to the high *S* value of the HT film, the power factor is also higher than that of the SCL film. It is worth noting that the σ value of the HT film starts to drop sharply above 180 °C in such a way that the value of the power factor also saturates and begins to decrease. The sudden drop of HT film at 210 °C probably arises from the oxidation of the film (Fig. S5 in the ESM). Comparing our current results with the ones obtained for polycrystalline Bi_2Te_3 film and ingot, our HT film shows superior power factor at RT, as presented in Fig. 7(d). Although the *S* value of the SCL film is relatively low, the high σ value ensures comparable power factor properties with the polycrystalline ingot (higher than hot pressed Bi_2Te_3 ingot [17]). For the HT film the *S* value is even slightly larger than that of the ingot, but the superior power factor can be almost completely attributed to the much higher conductivity in this thin film than in the ingot. In the polycrystalline film, a conductivity even lower than that in the polycrystalline ingot is observed, but in the films analyzed in the present work the conductivity is almost a factor of 3 to 4 times higher. Comparing some of the best power factors reported previously for Bi_2Te_3 materials, the power factor value of HT film at room temperature is very promising, because it is clearly higher than the ones of irradiated Bi_2Te_3 film (34 $\mu W \cdot cm^{-1} \cdot K^{-2}$) [13], comparable to epitaxial Bi_2Te_3 film (50 $\mu W \cdot cm^{-1} \cdot K^{-2}$) [42], and very close to one of bulk single crystal Bi_2Te_3 (58 $\mu W \cdot cm^{-1} \cdot K^{-2}$) [43].

4 Conclusions

In summary, we have deposited Bi_2Te_3 films with different nanostructured characteristics on Si wafer covered with native or thermal amorphous SiO_x layer, as well as crystalline mica. The results reveal that the Bi_2Te_3 layers grown on SiO_x are highly-textured with *c*-axis perpendicular to the surface, but show domains with random orientation parallel to the surface. Interestingly, XRD ω-rocking curve and TEM images show that the *c*-axis out-of-plane texture is slightly sharper for the film on thermal SiO_x than on native oxide. This is likely related to the stacking of two different domains in the vertical direction and also possible that the thermal oxide surface is slightly smoother compared to that of the native oxide. However, when the Bi_2Te_3 film is deposited on mica, it exhibits single-crystal-like structure with little defects, which can account for the high electrical conductivity (2,442 $S \cdot cm^{-1}$at RT). The Bi_2Te_3 film deposited on thermal oxide substrate shows a lower electrical conductivity (1,976 $S \cdot cm^{-1}$ at RT), due to the domains with random in-plane orientation, but still about three times higher than that of a normal polycrystalline film and ingot. Moreover, the domain boundaries with a high density of disordered stacking sequences including bilayer defects in the film on thermal oxide are considered responsible for the observed high Seebeck coefficient. In contrast, the Seebeck coefficient of the single-crystalline film is low. Thus, compared to a fully polycrystalline structure, the special nanostructure of the film on the thermal oxide gives rise to a higher power factor by increasing the electrical conductivity without any sacrifice in the Seebeck coefficient. The power factor of the single-crystal-like film remains similar to the ones of polycrystalline structure, because the large increase in conductivity is compensated by the lower Seebeck coefficient. The present work on chalcogenide thin films provides new insights and further scope to the optimization of thermoelectric properties by tailoring the texture and domain boundaries in such thin films.

Acknowledgements

We thank Hans de Vries for assisting in the operation of the pulsed laser deposition system. We are grateful to Prof. Beatriz Noheda for offering use of her lab facilities, in particular the setup for the van der Pauw measurements. We would also like to acknowledge the financial support from the China Scholarship Council, in particular for Heng Zhang's scholarship (No. 201706890019).

Electronic Supplementary Material: Supplementary material (please give brief details, e.g., further details of the annealing and oxidation procedures, STM measurements, AFM imaging and Raman spectroscopy measurements) is available in the online version of this article at https://doi.org/10.1007/s12274-021-3743-y.

References

[1] Poudel, B.; Hao, Q.; Ma, Y.; Lan, Y. C.; Minnich, A.; Yu, B.; Yan, X.; Wang, D. Z.; Muto, A.; Vashaee, D. et al. High-thermoelectric performance of nanostructured bismuth antimony telluride bulk alloys. *Science* **2008**, *320*, 634–638.

[2] Soni, A.; Zhao, Y. Y.; Yu, L. G.; Aik, M. K. K.; Dresselhaus, M. S.; Xiong, Q. H. Enhanced thermoelectric properties of solution grown $Bi_2Te_{3-x}Se_x$ nanoplatelet composites. *Nano Lett.* **2012**, *12*, 1203–1209.

[3] Fang, H. Y.; Bahk, J. H.; Feng, T. L.; Cheng, Z.; Mohammed, A. M. S.; Wang, X. W.; Ruan, X. L.; Shakouri, A.; Wu, Y. Thermoelectric properties of solution-synthesized n-type Bi_2Te_3 nanocomposites modulated by Se: An experimental and theoretical study. *Nano Res.* **2016**, *9*, 117–127.

[4] Hao, F.; Qiu, P. F.; Tang, Y. S.; Bai, S. Q.; Xing, T.; Chu, H. S.; Zhang, Q. H.; Lu, P.; Zhang, T. S.; Ren, D. D. et al. High efficiency Bi_2Te_3-based materials and devices for thermoelectric power generation between 100 and 300 °C. *Energy Environ. Sci.* **2016**, *9*, 3120–3127.

[5] Hao, F.; Xing, T.; Qiu, P. F.; Hu, P.; Wei, T. R.; Ren, D. D.; Shi, X.; Chen, L. D. Enhanced thermoelectric performance in n-type Bi_2Te_3-based alloys via suppressing intrinsic excitation. *ACS Appl. Mater. Interfaces* **2018**, *10*, 21372–21380.

[6] Snyder, G. J.; Toberer, E. S. Complex thermoelectric materials. *Nat. Mater.* **2008**, *7*, 105–114.

[7] Chowdhury, I.; Prasher, R.; Lofgreen, K.; Chrysler, G.; Narasimhan, S.; Mahajan, R.; Koester, D.; Alley, R.; Venkatasubramanian, R. On-chip cooling by superlattice-based thin-film thermoelectrics. *Nat. Nanotechnol.* **2009**, *4*, 235–238.

[8] Wu, Z. H.; Mu, E. Z.; Wang, Z. C.; Chen, X.; Wu, Z. M.; Liu, Y.; Hu, Z. Y. Bi_2Te_3 nanoplates' selective growth morphology on different interfaces for enhancing thermoelectric properties. *Cryst. Growth Des.* **2019**, *19*, 3639–3646.

[9] Le, P. H.; Liao, C. N.; Luo, C. W.; Leu, J. Thermoelectric properties of nanostructured bismuth-telluride thin films grown using pulsed laser deposition. *J. Alloys Compd.* **2014**, *615*, 546–552.

[10] Bassi, A. L.; Bailini, A.; Casari, C. S.; Donati, F.; Mantegazza, A.; Passoni, M.; Russo, V.; Bottani, C. E. Thermoelectric properties of Bi-Te films with controlled structure and morphology. *J. Appl. Phys.* **2009**, *105*, 124307.

[11] Lin, J. M.; Chen, Y. C.; Lin, C. P. Annealing effect on the thermoelectric properties of Bi_2Te_3 thin films prepared by thermal evaporation method. *J. Nanomater.* **2013**, *2013*, 201017.

[12] Fan, P.; Zhang, P. C.; Liang, G. X.; Li, F.; Chen, Y. X.; Luo, J. T.; Zhang, X. H.; Chen, S.; Zheng, Z. H. High-performance bismuth telluride thermoelectric thin films fabricated by using the two-step single-source thermal evaporation. *J. Alloys Compd.* **2020**, *819*, 153027.

[13] Suh, J.; Yu, K. M.; Fu, D. Y.; Liu, X. Y.; Yang, F.; Fan, J.; Smith, D. J.; Zhang, Y. H.; Furdyna, J. K.; Dames, C. et al. Simultaneous

enhancement of electrical conductivity and thermopower of Bi_2Te_3 by multifunctionality of native defects. *Adv. Mater.* **2015**, *27*, 3681–3686.

[14] Qiao, J. X.; Zhao, Y.; Jin, Q.; Tan, J.; Kang, S. Q.; Qiu, J. H.; Tai, K. P. Tailoring nanoporous structures in Bi_2Te_3 thin films for improved thermoelectric performance. *ACS Appl. Mater. Interfaces* **2019**, *11*, 38075–38083.

[15] Zeipl, R.; Walachová, J.; Pavelka, M.; Jelínek, M.; Studnička, V.; Kocourek, T. Power factor of very thin thermoelectric layers of different thickness prepared by laser ablation. *Appl. Phys. A* **2008**, *93*, 663–667.

[16] Vigil-Galán, O.; Cruz-Gandarilla, F.; Fandiño, J.; Roy, F.; Sastré-Hernández, J.; Contreras-Puente, G. Physical properties of Bi_2Te_3 and Sb_2Te_3 films deposited by close space vapor transport. *Semicond. Sci. Technol.* **2009**, *24*, 025025.

[17] Zhang, Z. W.; Wang, Y.; Deng, Y.; Xu, Y. B. The effect of (*00l*) crystal plane orientation on the thermoelectric properties of Bi_2Te_3 thin film. *Solid State Commun.* **2011**, *151*, 1520–1523.

[18] Jin, Q.; Shi, W. B.; Qiao, J. X.; Sun, C.; Tai, K. P.; Lei, H.; Jiang, X. Enhanced thermoelectric properties of bismuth telluride films with in-plane and out-of-plane well-ordered microstructures. *Scr Mater.* **2016**, *119*, 33–37.

[19] Saito, Y.; Fons, P.; Bolotov, L.; Miyata, N.; Kolobov, A. V.; Tominaga, J. A two-step process for growth of highly oriented Sb_2Te_3 using sputtering. *AIP Adv.* **2016**, *6*, 045220.

[20] Li, H. D.; Wang, Z. Y.; Kan, X.; Guo, X.; He, H. T.; Wang, Z.; Wang, J. N.; Wong, T. L.; Wang, N.; Xie, M. H. The van der Waals epitaxy of Bi_2Se_3 on the vicinal Si (111) surface: An approach for preparing high-quality thin films of a topological insulator. *New J. Phys.* **2010**, *12*, 103038.

[21] Saito, Y.; Fons, P.; Makino, K.; Mitrofanov, K. V.; Uesugi, F.; Takeguchi, M.; Kolobov, A. V.; Tominaga, J. Compositional tuning in sputter-grown highly-oriented Bi-Te films and their optical and electronic structures. *Nanoscale* **2017**, *9*, 15115–15121.

[22] Taskin, A. A.; Sasaki, S.; Segawa, K.; Ando, Y. Manifestation of topological protection in transport properties of epitaxial Bi_2Se_3 thin films. *Phys. Rev. Lett.* **2012**, *109*, 066803.

[23] Vermeulen, P. A.; Mulder, J.; Momand, J.; Kooi, B. J. Strain engineering of van der Waals heterostructures. *Nanoscale* **2018**, *10*, 1474–1480.

[24] Zhang, H.; Yimam, D. T.; de Graaf, S.; Momand, J.; Vermeulen, P. A.; Wei, Y. F.; Noheda, B.; Kooi, B. J. Strain relaxation in "2D/2D and 2D/3D systems": Highly textured mica/Bi_2Te_3, Sb_2Te_3/Bi_2Te_3, and Bi_2Te_3/GeTe heterostructures. *ACS Nano* **2021**, *15*, 2869–2879.

[25] Rijnders, G.; Blank, D.H. A. *In situ* diagnostics by high-pressure RHEED during PLD. In *Pulsed Laser Deposition of Thin Films*: *Applications-Led Growth of Functional Materials*. Eason, R., Ed.; John Wiley & Sons, Inc.: Hoboken, 2007; pp 85-97.

[26] Tang, F.; Parker, T.; Wang, G. C.; Lu, T. M. Surface texture evolution of polycrystalline and nanostructured films: RHEED surface pole figure analysis. *J. Phys. D:. Appl. Phys.* **2007**, *40*, R427–R439.

[27] Ning, J.; Martinez, J. C.; Momand, J.; Zhang, H.; Tiwari, S. C.; Shimojo, F.; Nakano, A.; Kalia, R. K.; Vashishta, P.; Branicio, P. S. et al. Differences in Sb_2Te_3 growth by pulsed laser and sputter deposition. *Acta Mater.* **2020**, *200*, 811–820.

[28] Kim, Y.; Cho, S.; DiVenere, A.; Wong, G. K. L.; Ketterson, J. B. Composition-dependent layered structure and transport properties in BiTe thin films. *Phys. Rev. B* **2001**, *63*, 155306.

[29] Takagaki, Y.; Jenichen, B.; Kopp, V.; Jahn, U.; Ramsteiner, M.; Herrmann, C. Semicoherent growth of Bi_2Te_3 layers on InP substrates by hot wall epitaxy. *Semicond. Sci. Technol.* **2014**, *29*, 075021.

[30] Boschker, J. E.; Tisbi, E.; Placidi, E.; Momand, J.; Redaelli, A.; Kooi, B. J.; Arciprete, F.; Calarco, R. Textured Sb_2Te_3 films and GeTe/Sb_2Te_3 superlattices grown on amorphous substrates by molecular beam epitaxy. *AIP Adv.* **2017**, *7*, 015106.

[31] Harrison, S. E.; Li, S.; Huo, Y.; Zhou, B.; Chen, Y. L.; Harris, J. S. Two-step growth of high quality Bi_2Te_3 thin films on Al_2O_3(0001) by molecular beam epitaxy. *Appl. Phys. Lett.* **2013**, *102*, 171906.

[32] Lotnyk, A.; Hilmi, I.; Ross, U.; Rauschenbach, B. Van der Waals interfacial bonding and intermixing in GeTe-Sb_2Te_3-based superlattices. *Nano Res.* **2018**, *11*, 1676–1686.

[33] Borisova, S.; Krumrain, J.; Luysberg, M.; Mussler, G.; Grützmacher, D. Mode of growth of ultrathin topological insulator Bi_2Te_3 films on Si (111) substrates. *Cryst. Growth Des.* **2012**, *12*, 6098–6103.

[34] Momand, J.; Lange, F. R. L.; Wang, R. N.; Boschker, J. E.; Verheijen, M. A.; Calarco, R.; Wuttig, M.; Kooi, B. J. Atomic stacking and van-der-Waals bonding in GeTe-Sb_2Te_3 superlattices. *J. Mater. Res.* **2016**, *31*, 3115–3124.

[35] Ross, U.; Lotnyk, A.; Thelander, E.; Rauschenbach, B. Microstructure evolution in pulsed laser deposited epitaxial Ge-Sb-Te chalcogenide thin films. *J. Alloys Compd.* **2016**, *676*, 582–590.

[36] Wang, N.; Chen, H. J.; He, H. C.; Norimatsu, W.; Kusunoki, M.; Koumoto, K. Enhanced thermoelectric performance of Nb-doped $SrTiO_3$ by nano-inclusion with low thermal conductivity. *Sci. Rep.* **2013**, *3*, 3449.

[37] Alam, H.; Ramakrishna, S. A review on the enhancement of figure of merit from bulk to nano-thermoelectric materials. *Nano Energy* **2013**, *2*, 190–212.

[38] Bando, H.; Koizumi, K.; Oikawa, Y.; Daikohara, K.; Kulbachinskii, V. A.; Ozaki, H. The time-dependent process of oxidation of the surface of Bi_2Te_3 studied by X-ray photoelectron spectroscopy. *J. Phys.: Condens. Matter* **2000**, *12*, 5607–5616.

[39] Goldsmid, H. J. *Thermoelectric Refrigeration*; Temple Press Books: London, 1964.

[40] Deng, Y.; Zhang, Z. W.; Wang, Y.; Xu, Y. B. Preferential growth of Bi_2Te_3 films with a nanolayer structure: Enhancement of thermoelectric properties induced by nanocrystal boundaries. *J. Nanopart. Res.* **2012**, *14*, 775.

[41] Mao, J.; Wu, Y. X.; Song, S. W.; Zhu, Q.; Shuai, J.; Liu, Z. H.; Pei, Y. Z.; Ren, Z. F. Defect engineering for realizing high thermoelectric performance in n-type Mg_3Sb_2-based materials. *ACS Energy Lett,* **2017**, *2*, 2245–2250.

[42] Nurnus, J.; Bottner, H.; Beyer, H.; Lambrecht, A. Epitaxial bismuth telluride layers grown on [111] barium fluoride substrates suitable for MQW-growth. In *Eighteenth International Conference on Thermoelectrics. Proceedings, ICT'99(Cat. No.99TH8407)*, Baltimore, 1999, pp 696-699.

[43] Rowe, D.M. *CRC Handbook of Thermoelectrics*, CRC Press: Boca Raton, 1995.

[44] Bos, J. W. G.; Zandbergen, H. W.; Lee, M. H.; Ong, N. P.; Cava, R. J. Structures and thermoelectric properties of the infinitely adaptive series $(Bi_2)_m(Bi_2Te_3)_n$. *Phys. Rev. B* **2007**, *75*, 195203.